



10). This imbalance results in recruitment of a large number of neutrophils and other immune cells to the respiratory tract (11–15).

For reasons that remain somewhat unclear, SARS-CoV-2 infections can exhibit substantial disease heterogeneity (16–18). Although many individuals are asymptomatic or report mild flu-like symptoms, a subset of individuals, especially those who are aged or have underlying comorbidities, experience considerable morbidity and mortality that can include nonpulmonary complications (19, 20). Complications of viral infection in these populations can include cardiac abnormalities, cognitive impairment, and/or gastrointestinal issues, among other pathologies, leading many to suggest that distal sites of replication may contribute to the severity of COVID-19 (21–25). In an effort to better understand the systemic nature of the disease, we chose to study SARS-CoV-2 infection in the golden hamster model, which phenocopies many aspects of COVID-19 (14, 26–29). Here, we characterized the early systemic response to SARS-CoV-2 under physiological conditions and how it was affected when the immune response was either dampened or bypassed altogether. These data demonstrated that systemic antiviral signaling was the by-product of lung-derived engagement of the immune system, which, when compromised, resulted in viremia and de novo infection of distal organs. Together, these results advance our understanding as it relates to the diverse extrapulmonary clinical presentations that can materialize after a respiratory virus infection.

## RESULTS

### SARS-CoV-2 infection induces an antiviral response in peripheral organs

To characterize the systemic transcriptional response after SARS-CoV-2 infection, we performed bulk RNA sequencing (RNA-seq) of a panel of organs derived from a cohort of 6-week-old male golden hamsters intranasally infected with 1000 plaque-forming units (PFU) of SARS-CoV-2 at 3 days postinfection (dpi). Alignment of RNA-seq data from olfactory bulb (O.B.), whole brain, liver, kidney, gastrointestinal tract (G.I.), pancreas, spleen, heart, and lung demonstrated organ-specific transcriptional clustering (fig. S1A). Comparing mock-treated to infected tissue-matched samples revealed a diverse list of differentially expressed genes (DEGs), implicating many shared transcriptional responses across organs, including evidence for extensive cytokine signaling and induction of numerous stress responses such as hypoxia and the unfolded protein response (fig. S1B and data file S1). The most dominant among the enriched annotations after SARS-CoV-2 infection were the transcriptional signatures associated with IFN-I/III signaling, which were independently corroborated by reverse transcription quantitative polymerase chain reaction (RT-qPCR) analysis of *Isg15* (Fig. 1A and fig. S1C).

To assess the relation between the IFN-I/III signature and the presence of infectious virus, we next performed plaque assays from these same samples (Fig. 1B). Consistent with the findings of others (14, 15, 26, 30), we observed high levels of replication-competent virus in the lungs of all inoculated animals, with titers  $\sim 10^6$  PFU/ml. Infectious virus was also readily obtained from the O.B. and less consistently from the heart (Fig. 1B). In addition, infectious virus from the G.I. tract of an individual hamster was also detected, possibly a result of ingesting the inoculum (Fig. 1B). Given the juxtaposition of the host antiviral response in the absence of

infectious material, we assessed the presence of SARS-CoV-2 genomic RNA at 3 dpi by RT-qPCR analysis using Centers for Disease Control and Prevention (CDC)-validated primers and probe (31). Elevated virus RNA levels were largely restricted to the lung, thus corroborating our plaque assays (fig. S1D). For all other tissues examined but the G.I. tract, the RNA levels were not significantly different than the background noise picked up in mock samples and thus were considered negative. To ensure that the host IFN response did not reflect a transient dissemination of virus that was simply cleared by 3 dpi, we repeated this experiment but examined animals at 1 dpi (Fig. 1C). In agreement with our observations at 3 dpi, we found SARS-CoV-2 infectious material to be largely confined to the airways. Last, to analyze the systemic IFN response independently of RNA analysis, we performed immunohistochemistry for the ISG product Mx (9) and SARS-CoV-2 N protein on both lung and kidney sections at 3 dpi (Fig. 1D). These data provided additional evidence that SARS-CoV-2 infection not only was retained in the airways but also induced an antiviral response in additional distal tissues, as shown by detection of Mx protein in both lung and kidney. Together, these data suggest that the systemic antiviral signatures observed after SARS-CoV-2 infection for most tissues are not the result of a productive infection. Given this result, we hypothesized that the observed uniform engagement of the antiviral response could result from a by-product of active replication in the lung of a viral and/or host nature, such as infectious virus or cytokines, that enters circulation and disseminates systemically, inducing the observed antiviral response.

### Evidence for IFN-I/III signaling in circulating blood early during infection

To explore this hypothesis further and characterize circulation dynamics in vivo, we infected hamsters intranasally and collected whole blood and corresponding lung tissue 1 and 3 dpi. Despite harboring titers in the respiratory tract exceeding  $10^6$  PFU/ml at these time points, none of the infected animals exhibited evidence of replication-competent material from heparin-treated blood at either time point (fig. S2A). Next, we attempted to detect viral RNA in these samples. RT-qPCR analysis consistently detected low levels of SARS-CoV-2 N in the blood only at 1 dpi even in the absence of infectious material (fig. S2B). We next performed RNA-seq analysis on whole blood samples to assess DEGs between mock and infected animals (data file S2). In agreement with our earlier characterization of distal tissues, the cells found in whole blood also demonstrated a statistically enriched ISG signature at both 1 and 3 dpi, as exemplified by *Ifit3*, *Mx*, *Isg15*, *Oasl*, and *Irf7* (Fig. 2, A and B).

The transcriptional induction of ISGs can be directly mediated by virus infection or by IFN-I/III signaling (32). Transcripts that enable parsing of these overlapping transcriptomes include *Mx*, which is uniquely induced by IFN signaling and was readily detected in both blood and lung samples by RNA-seq, immunohistochemical, and RT-qPCR analyses (Fig. 1, A and D, and fig. S2C). In addition, the presence of *Ifna*, *Ifnb*, or *Ifnl* transcripts can serve as a surrogate for virus infection, because their transcriptional induction initiates only upon direct detection of SARS-CoV-2-mediated dsRNA (33, 34). To ascertain whether the ISG signature in whole blood derived from a response to a circulating host factor or to the direct sensing of virus or virus-derived debris, we analyzed whole blood and lung tissue for the presence of *Ifnb* or *Ifnl* reads.

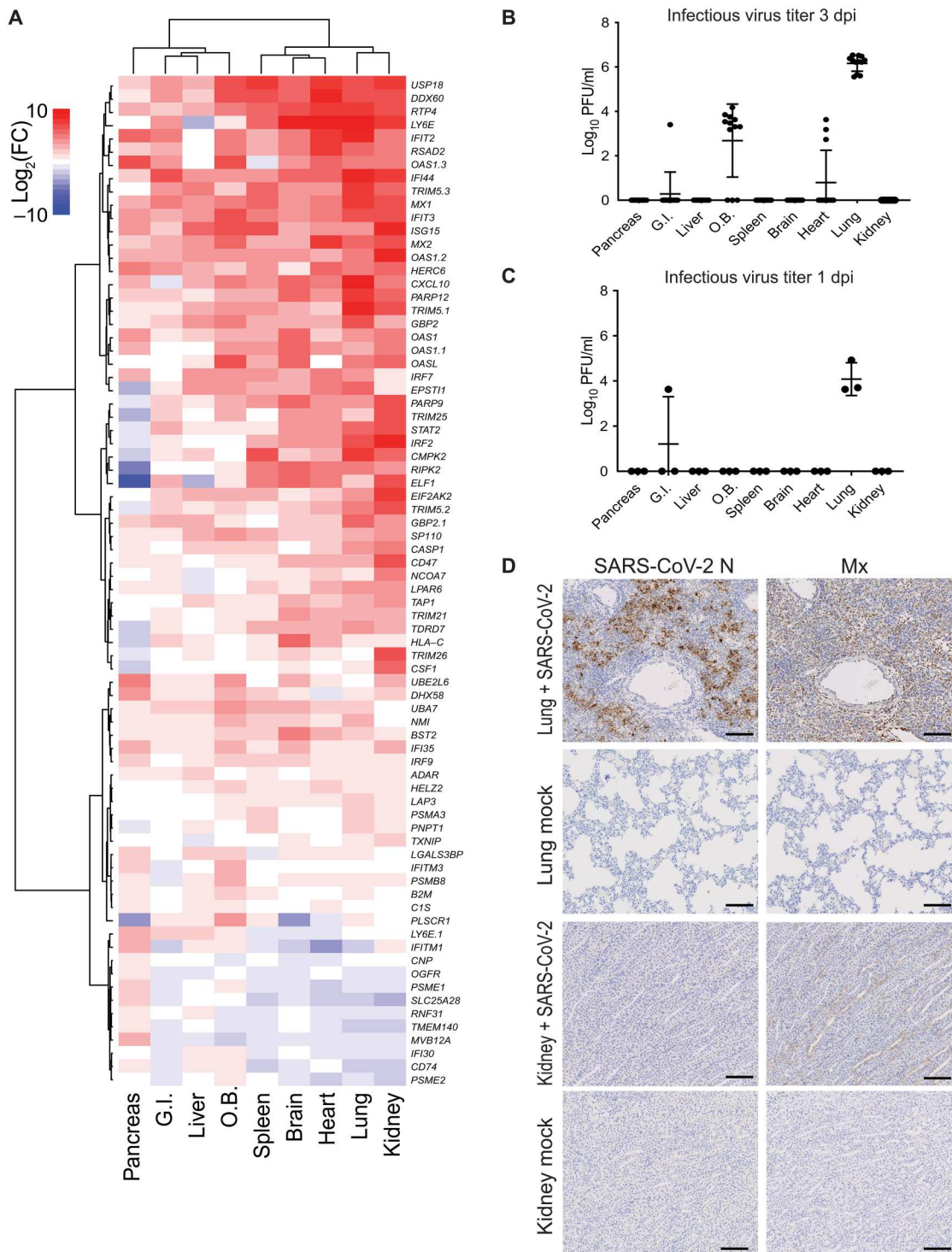


**Fig. 1. SARS-CoV-2 infection induces an IFN signaling response in peripheral organs.** (A) Heatmap depicting the expression levels of DEGs ( $P$ -adjusted value < 0.05) belonging to the IFN-I response (Hallmark IFN- $\alpha$  response) for selected tissues.  $\log_2(\text{fold change})$  [ $\log_2(\text{FC})$ ] values were calculated from RNA-seq analyses of tissues from SARS-CoV-2 intranasally infected (1000 PFU, 3 dpi) and mock-treated hamsters ( $n = 3$  animals per group). (B) Viral load as determined by plaque assay using tissue homogenates from golden hamsters infected intranasally with 1000 PFU of SARS-CoV-2 and collected 3 dpi. Values express the  $\log_{10}$  PFU/ml. Limit of detection, 200 PFU/ml. Means and SDs from 12 independent biological replicates per group are shown. (C) Viral load as determined by plaque assay using tissue homogenates from golden hamsters infected intranasally with 1000 PFU of SARS-CoV-2 and collected 1 dpi. Values are expressed  $\log_{10}$  PFU/g. Limit of detection, 200 PFU/g. Means and SDs from three independent biological replicates per group are shown. (D) Representative images of lung and kidney from golden hamsters intranasally infected with SARS-CoV-2 (1000 PFU, 3 dpi) and stained for SARS-CoV-2 N (left) or Mx (right) ( $n = 4$  animals per group). Scale bars, 100  $\mu\text{m}$ .

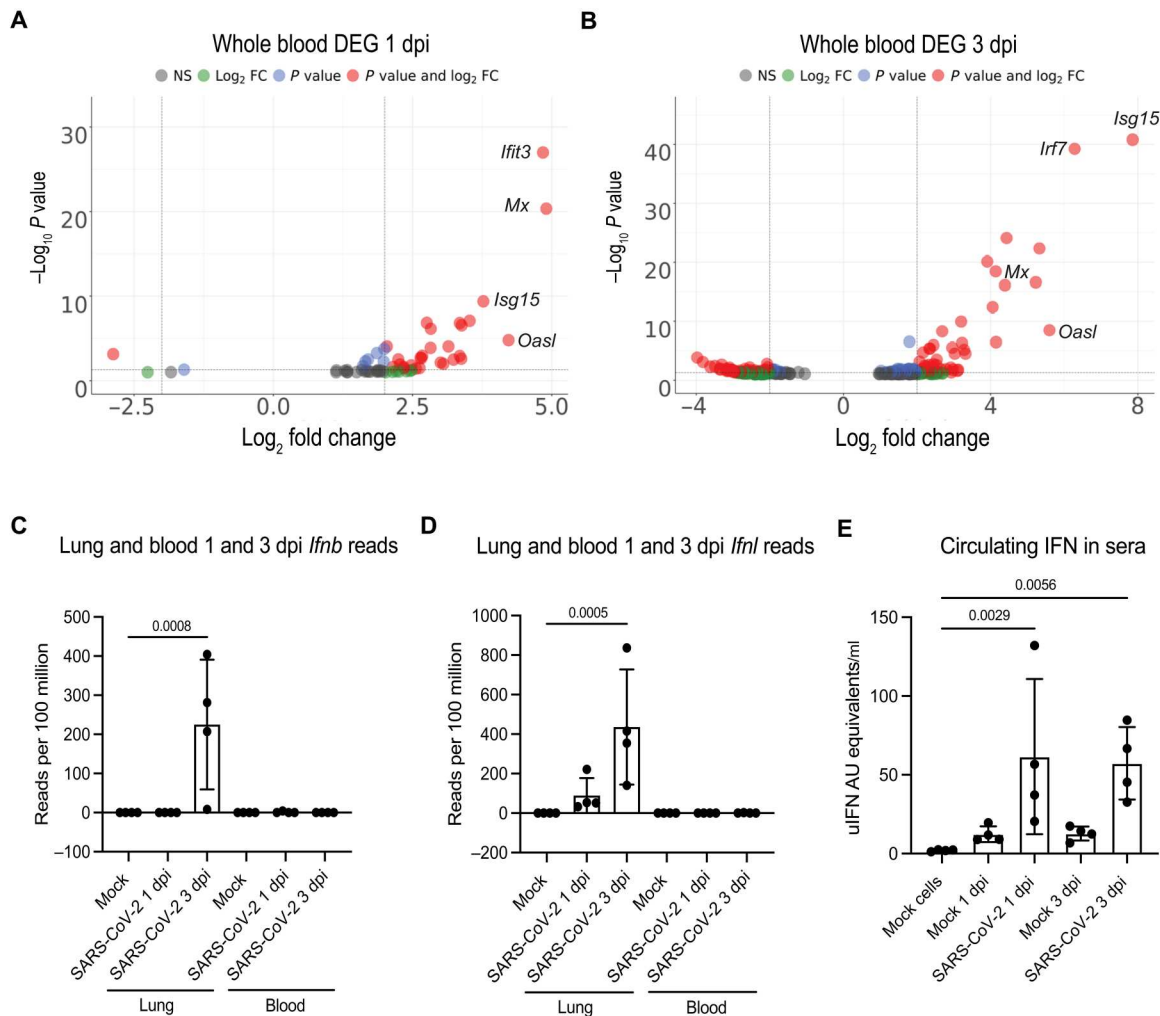


**Fig. 2. An antiviral transcriptional signature is detected in circulating blood early during infection.** (A and B) Volcano plot for DEGs in whole blood of golden hamsters ( $n = 4$  animals per group) infected with 1000 PFU of SARS-CoV-2 at 1 (A) and 3 (B) dpi. Gray, not significant (NS); blue, significant; red, significant and  $\log_2$  fold change (FC)  $> 2$ . Relevant genes to the IFN-I-dependent antiviral response are noted and labeled by their human ortholog. (C and D) Relative amounts of IFN- $\beta$  gene (*Ifnb*) or IFN- $\lambda$  gene (*Ifnl*) RNA present at 1 or 3 dpi in the blood or lungs of SARS-CoV-2 infected (1000 PFU) or mock-treated animals. RNA amount was calculated from the number of sequencing reads that aligned to *Ifnb* (C) or *Ifnl* (D) and normalized for every 100 million transcripts. Error bars represent SD from four independent biological replicates per group. RPM, reads per million. Ordinary one-way analysis of variance (ANOVA) with Dunnett's multiple comparisons test with a single pooled variance; significant  $P$  values are indicated. (E) Indirect quantification of circulating IFN in the sera of SARS-CoV-2 intranasally infected (1000 PFU) or mock-infected animals at 1 and 3 dpi. BHK-21 cells were incubated with sera from infected and control animals for 16 hours, and the induction of *Mx* was quantified by RT-qPCR analysis. Increasing amounts of exogenous universal IFN (uIFN) were included to generate a standard curve, and uIFN arbitrary unit equivalents (uIFN AU equivalents/ml) were calculated by linear regression. Values are expressed as uIFN AU equivalents per ml calculated from the induction of the *Mx* gene over control cells by the  $\Delta\Delta C_t$  method. Error bars represent SD from four independent biological replicates per group. Ordinary one-way ANOVA with Dunnett's multiple comparisons test with a single pooled variance; significant  $P$  values are indicated.

These data showed the presence of *Ifnl* at 1 dpi, which increased by 3 dpi in the lung, whereas *Ifnb* induction was evident only at 3 dpi (Fig. 2, C and D), consistent with the delayed antiviral response previously documented for SARS-CoV-2 infection (6, 14, 35). We were unable to detect *Ifna* transcripts in any samples, possibly a reflection of the incomplete or incorrect annotation of this gene family in the hamster genome, because this locus is highly variable and repetitive in all vertebrates (36). Moreover, we could not identify reads aligning to the *Ifna*, *Ifnb*, or *Ifnl* genes in any of the blood samples, indicating that ISG induction is the product of IFN-I/III signaling as opposed to direct viral sensing. Direct evidence for circulating IFN-

I and/or IFN-III should be possible; however, a lack of commercial reagents for hamsters precluded our ability to measure these directly. Instead, we developed a bioassay to indirectly assess the presence of IFNs by testing the ability of sera collected at 1 and 3 dpi to induce *Mx* transcription in the baby hamster kidney (BHK-21) fibroblast cell line. Because these cells lack the ability to produce IFN-I/III, *Mx* induction serves as a proxy for their direct presence in the sera (37). To gain further insight from this assay, we also generated a standard curve by measuring *Mx* expression in BHK-21 cells treated with increasing units of recombinant universal IFN, which exhibits activity among multiple species. These efforts allowed us to estimate

standardized IFN units present in the serum from *Mx* induction on cells. IFN-I/III signaling was evident at 1 dpi at ~60 U/ml, with levels remaining stable at 3 dpi (Fig. 2E). Collectively, these data support the model that SARS-CoV-2 infection generates IFN-I and/or IFN-III in the lungs, which then enters the circulation and primes organs to enhance their antiviral defenses.

### Impairing immune priming increases SARS-CoV-2 infection of peripheral organs

Deficits in innate immune signaling result in more severe clinical presentations among patients with COVID-19 (38). This phenomenon has also been reported in hamsters, where genetic ablation of IFN-I but not IFN-III signaling increased the amount of viral RNA present during infection (29). Although these studies demonstrate the importance of IFN signaling in COVID-19 pathology, systems in which the IFN system is completely absent or disabled are unlikely to further inform the contribution of antiviral priming to disease progression. We addressed this issue using dexamethasone, a glucocorticoid that suppresses *de novo* gene transcription, to dampen the host immune response to SARS-CoV-2 (39). Because SARS-CoV-2 can replicate in most tissues *ex vivo* despite little evidence for these same observations *in vivo* (40, 41), we hypothesized that system-wide priming may contribute to preventing viral dissemination and/or consequent infection of peripheral organs. To test this hypothesis as it relates to infectious virus, we analyzed the effect of administering dexamethasone daily to hamsters infected intranasally with SARS-CoV-2 to reduce distal inflammation to baseline levels. Corroborating published data, we found that SARS-CoV-2 titers were maintained in vehicle-treated animals at levels between  $10^6$  and  $10^7$  PFU/ml for the initial 5 days after challenge and subsequently cleared thereafter (Fig. 3A) (14, 15, 30, 42). Similarly, dexamethasone treatment did not affect virus titers in the lung during the first 3 days of infection (Fig. 3A). However, dexamethasone-treated animals failed to control virus replication thereafter because titers continued to rise after 3 dpi, and replication-competent virus was maintained through 7 dpi and lastly cleared by 9 dpi (Fig. 3A). Histological analyses of SARS-CoV-2 N and host *Mx* protein expression in the lungs of vehicle- and dexamethasone-treated animals confirmed comparable virus levels at 3 dpi but a reduction in antiviral defenses as denoted by decreased *Mx* count in dexamethasone-treated animals (Fig. 3B and fig. S3A).

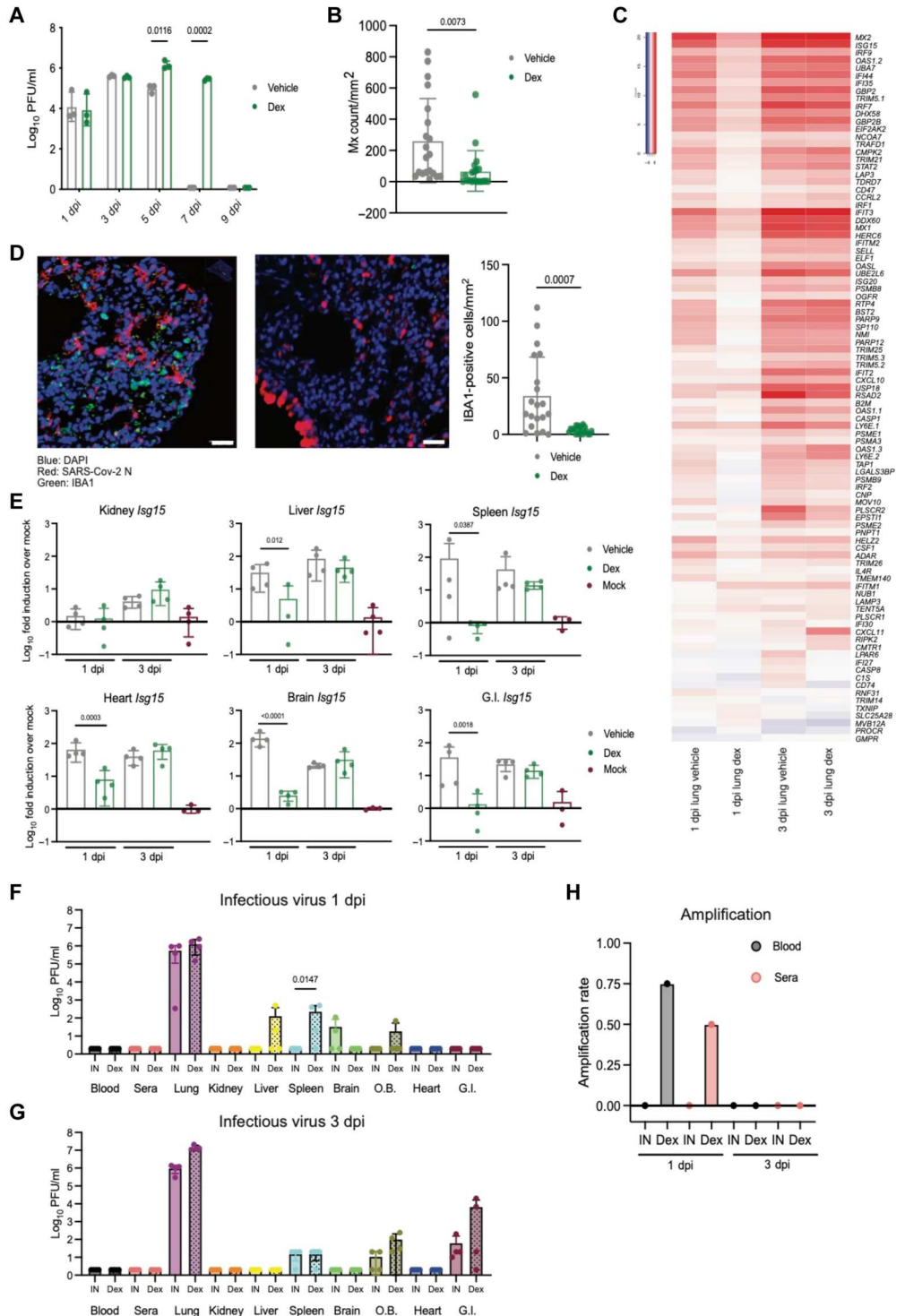
To better understand the underlying biology responsible for the delay in virus clearance, we compared the host transcriptional response in the lungs of vehicle- and dexamethasone-treated animals (Fig. 3C). We chose 1 and 3 dpi time points to avoid the possibility that differences in viral load might confound our results. RNA-seq analysis of total lung samples showed that dexamethasone treatment significantly delayed ISG production in the respiratory tract without affecting other aspects of host biology (Fig. 3C and data file S3). Furthermore, we performed flow cytometry on total lung cells to better characterize the impact of dexamethasone on immune cell populations across experimental cohorts. Analyses of lung samples from mock-treated or SARS-CoV-2-infected hamsters demonstrated a reduction in B cell populations, defined as  $CD3^-$ /major histocompatibility complex II (MHCII)<sup>+</sup> (fig. S3B). T cells, defined as  $CD3^+$ /MHCII<sup>-</sup>, did not show overt changes after dexamethasone treatment in the absence of infection, but there was a significant decrease in T cell frequency after SARS-CoV-2 challenge (fig. S3C). Moreover, immunofluorescence

staining with an antibody specific for ionized calcium-binding adaptor molecule 1 (IBA1), a molecular marker for phagocytic cells such as macrophages and dendritic cells, revealed that dexamethasone-treated animals exhibited significantly diminished levels of infiltrating cells (Fig. 3D) (43). Together, these data support the ability of corticosteroids such as dexamethasone to diminish the host response to SARS-CoV-2, resulting in prolonged infection and delayed innate and adaptive immune responses. These results are consistent with case reports of immunocompromised individuals showing sustained SARS-CoV-2 replication in the lung (44).

Having confirmed that dexamethasone treatment reduced innate immune induction in response to SARS-CoV-2 infection in the lung, we next tested the impact of this treatment on peripheral organs. We postulated that circulating levels of IFN-I/III induced an antiviral response in extrapulmonary organs that may serve to restrict virus tropism, an observation previously reported after ablation of signal transducer and activator of transcription 2, a pivotal component of the IFN-I/III signaling pathways (29). If this systemic inflammation protects peripheral organs against viral infection, we reasoned that dexamethasone treatment, which dampens this response, should then result in higher levels of infectious material not only in the lung but also elsewhere in the body. Hamsters were infected with 1000 PFU intranasally and treated daily with dexamethasone starting from day 0 (fig. S3D). To initially assess the level of IFN-I priming in dexamethasone-treated animals, we measured *Isg15* expression as a proxy for IFN signaling in the kidney, liver, G.I. tract, brain, and heart at 1 and 3 dpi, because this was one of the more prominent ISGs found in all tissues (Figs. 1A and 3E). Similar to what was observed in the lung, dexamethasone treatment diminished the induction of *Isg15* at 1 dpi in most organs tested from infected animals (Fig. 3E). At 3 dpi, *Isg15* expression in dexamethasone-treated animals was similar to that in vehicle-treated animals, despite repeated drug treatments (Fig. 3E). To assess whether this delay in IFN-I/III priming resulted in virus dissemination beyond the airways, we again performed plaque assays on blood and tissues from these cohorts, which detected the presence of infectious SARS-CoV-2 in the lungs, livers, spleens, O.B.s, and G.I. tracts of infected animals treated with dexamethasone, albeit not with complete penetrance, suggesting that IFN-I/III priming affected the tropism of the virus (Fig. 3, F and G). However, plaque assays performed on blood or sera failed to detect infectious material, raising the question as to the compartment through which viral dissemination was occurring. To pursue this question, we attempted to amplify infectious virus from blood and sera by performing an additional amplification cycle in the highly permissive Vero E6 cell line (Fig. 3H) (45). This technique allows for the theoretical detection of a single PFU, because we provided 48 hours for the virus to gain entry and replicate in cell culture. Plaque assays of the supernatants of amplified samples enabled us to detect low-level viremia in ~50 to 75% of dexamethasone-treated animals only at 1 dpi and thus provided additional evidence that SARS-CoV-2 could become viremic and subsequently infect distal organs in the absence of a robust antiviral response (Fig. 3H). In agreement with these findings, we noted that animals in which no infectious material could be detected in the blood or sera at 1 dpi were also negative by plaque assay when examining the corresponding kidney, liver, spleen, heart, and G.I. tract samples (Fig. 3, F and G).

**Fig. 3. Impairing immune priming increases SARS-CoV-2 infection of peripheral organs.**

**(A)** Viral loads determined by plaque assay in the lungs of animals intranasally infected with SARS-CoV-2 (1000 PFU) and treated with vehicle (gray) or dexamethasone (green) at 1, 3, 5, 7, and 9 dpi. Values are expressed as  $\log_{10}$  PFU/ml. Limit of detection, 20 PFU/g. Mean and SDs from three biological replicates per group is shown. Ordinary one-way ANOVA with Šidák's multiple comparisons test with a single pooled variance; significant *P* values are indicated. **(B)** Counts of Mx-positive cells per  $\text{mm}^2$  from images of lungs stained with Mx-specific antibodies by immunohistochemistry (five representative images per lung,  $n = 4$  animals per group). Lung tissue was harvested from golden hamsters intranasally infected with SARS-CoV-2 (1000 PFU, 3 dpi) and treated with vehicle or dexamethasone at 1 and 3 dpi.  $\log_2$ (fold change) values were calculated from RNA-seq analyses of SARS-CoV-2-infected (1000 PFU) compared with mock-treated hamster tissues ( $n = 4$  animals per group). **(D)** Immunofluorescence images of representative lung tissue from golden hamsters intranasally infected with SARS-CoV-2 (1000 PFU, 3 dpi) and treated with vehicle (left) or dexamethasone (middle). Lung tissue was stained with fluorescent antibodies specific for SARS-CoV-2 N (red), the pan-macrophage marker IBA1 (green), and nuclei were stained with 4',6'-diamidino-2-phenylindole (DAPI) (blue) ( $n = 4$  animals per condition). Counts of IBA1-positive cells per  $\text{mm}^2$  (right) from lungs that were harvested from golden hamsters intranasally infected with SARS-CoV-2 (1000 PFU, 3 dpi) and treated with vehicle or dexamethasone. Lung tissue was stained with fluorescent antibodies specific for SARS-CoV-2 N (red), the pan-macrophage marker IBA1 (green), and nucleus DAPI (blue) and visualized by immunofluorescent microscopy (five representative images per lung,  $n = 4$  animals per group). Unpaired *t* test with Welch's correction; significant *P* values are indicated. Scale bars, 20  $\mu\text{m}$ . **(E)** RT-qPCR analysis with primers specific for *Isg15* on RNA extracted from kidneys, livers, spleens, hearts, brains, and G.I. tracts of mock- or SARS-CoV-2-infected animals that were vehicle- or dexamethasone-treated at 1 or 3 dpi. Values are expressed as the  $\log_{10}$  fold induction in expression over mock calculated by the  $\Delta\Delta\text{Ct}$  method. Error bars represent SD from four independent biological replicates per group. Ordinary one-way ANOVA with Šidák's multiple comparisons test with a single pooled variance; significant *P* values are indicated. **(F and G)** Viral loads determined by plaque assays performed on blood, lung, kidney, liver, spleen, brain, O.B., heart, G.I. and sera samples from SARS-CoV-2-infected animals that were treated with vehicle [intranasally (IN)] or dexamethasone (Dex) at 1 (F) and 3 (G) dpi. Individual dots represent individual animals ( $n = 4$  animals per group per time point). Values are expressed as  $\log_{10}$  PFU/ml. Limit of detection, 20 PFU/ml. Kruskal-Wallis with uncorrected Dunn's test; significant *P* values are indicated. **(H)** Proportion of blood and sera samples that were positive for infectious virus after direct amplification on Vero E6 cells. Samples were collected from animals intranasally infected with 1000 PFU of SARS-CoV-2 and treated with vehicle (IN) or dexamethasone at 1 or 3 dpi as indicated ( $n = 4$  animals per group per time point).



Downloaded from https://www.science.org on February 01, 2024

### Lung-mediated antiviral priming protects the host from SARS-CoV-2 dissemination

The capacity of SARS-CoV-2 to become viremic after a diminished innate immune response may, in part, explain both the heterogeneity of COVID-19 symptoms and sequelae as well as why age and other factors that can affect the strength of the immune response are prominent comorbidities associated with more severe outcomes. For example, the capacity of a respiratory virus to be associated with cardiac arrhythmias, hyperglycemia, adipose inflammation, petechiae, elevated bilirubin, and/or acute kidney injury is seemingly paradoxical (18). However, this could be explained by individuals who fail to induce an adequate innate immune response in the lungs, resulting in a low level of viremia that can seed infections in distal tissues. This latter idea is supported by findings that autoantibodies to IFN-I are associated with critical disease outcomes and can aid in explaining how infectious virus can be isolated in distal tissues in some hospital settings as well as in the aged population, who exhibit diminished IFN signaling capacity (19, 25, 46).

To explore this concept further, we administered SARS-CoV-2 intravenously to entirely bypass lung immune control (Fig. 4, A and B, and fig. S4A). Assessment of infectious virus by plaque assay revealed detectable levels of SARS-CoV-2 at 1 dpi in both sera and blood, which was cleared by 3 dpi. This direct induction of viremia resulted in consistent infections by 3 dpi in the lung and kidney, as well as the liver, spleen, heart, and G.I. tract, albeit at low levels (Fig. 4B). In the kidneys, titers were maintained at  $\sim 10^4$  PFU/ml at 1 and 3 dpi (Fig. 4, A and B). To confirm that titers in the kidney reflected bona fide infection, we analyzed fixed tissue by immunohistochemistry for N and Mx protein levels, which revealed SARS-CoV-2-positive parenchymal cells of the kidney and endothelial cells within the peritubular capillary network and renal medulla (Fig. 4C and fig. S4B). Moreover, surrounding tissue areas also showed elevated levels of Mx staining, suggesting host antiviral engagement (Fig. 4D and fig. S4B). These observations were independently verified by immunofluorescent staining of N and Mx in kidney tissue from SARS-CoV-2-infected animals (Fig. 4, E and F). Using our bioassay in BHK-21 cells to evaluate the circulating levels of IFN-I/III after virus administration, we found that, compared with intravenous infection, intranasal infection generated more systemic signaling at 1 dpi but comparable levels at 3 dpi (Fig. 4, G and H). These data suggest that productive infection of the lung was a more critical generator of systemic IFN signaling. This concept is supported by the observation that a single animal within the intravenously infected cohort that showed infectious SARS-CoV-2 in the lung at 1 dpi also generated the highest levels of circulating IFN-I/III (Fig. 4, A and G).

To formally evaluate the correlation between systemic IFN-I/III production and the presence of infectious virus, we performed a meta-analysis on previously collected data to compare how the presence of infectious virus within the lung or kidney of a given hamster compared with the quantified amount of IFN-I/III in circulation of that same hamster. This analysis showed that circulating IFN was detected only in animals with positive lung titers, independently of the route of inoculation (Fig. 4I). To further explore whether this phenotype was strictly defined by lung infectivity, we performed the same analysis on animals for which the data were stratified for infectious material in the kidney. In contrast to what was observed in the airways, the viral load in the kidney did not affect levels of circulating IFN-I/III (Fig. 4J). These data demonstrate that

circulating IFN responses to SARS-CoV-2 are a distinct product of respiratory infection and may be uniquely capable of protecting distal organs. To determine whether the kidneys respond to infectious virus in a more localized manner, we next performed RNA-seq analyses on kidneys of intranasally and intravenously infected cohorts (fig. S4C and data file S4), which revealed that the ISG profile in the kidneys was similar for the most highly expressed and canonical ISGs (*Isg15*, *Usp18*, *Mx2*, *Oas1.3*, *Rtp4*, *Ifit3*, and *Irf7*) regardless of route of virus administration. This result provided additional evidence that the response in the airways can produce distal protection that is analogous to what an organ may generate after a localized infection (fig. S4C). To further evaluate this concept, we assessed the correlation between antiviral signaling and infectious material in either the lung or the kidney, which demonstrated that systemic antiviral signaling, as calculated from RNA-seq data and defined as RNA-seq IFN score, was observed only during respiratory infection regardless of the tissue examined (Fig. 4, K and L, and fig. S4D).

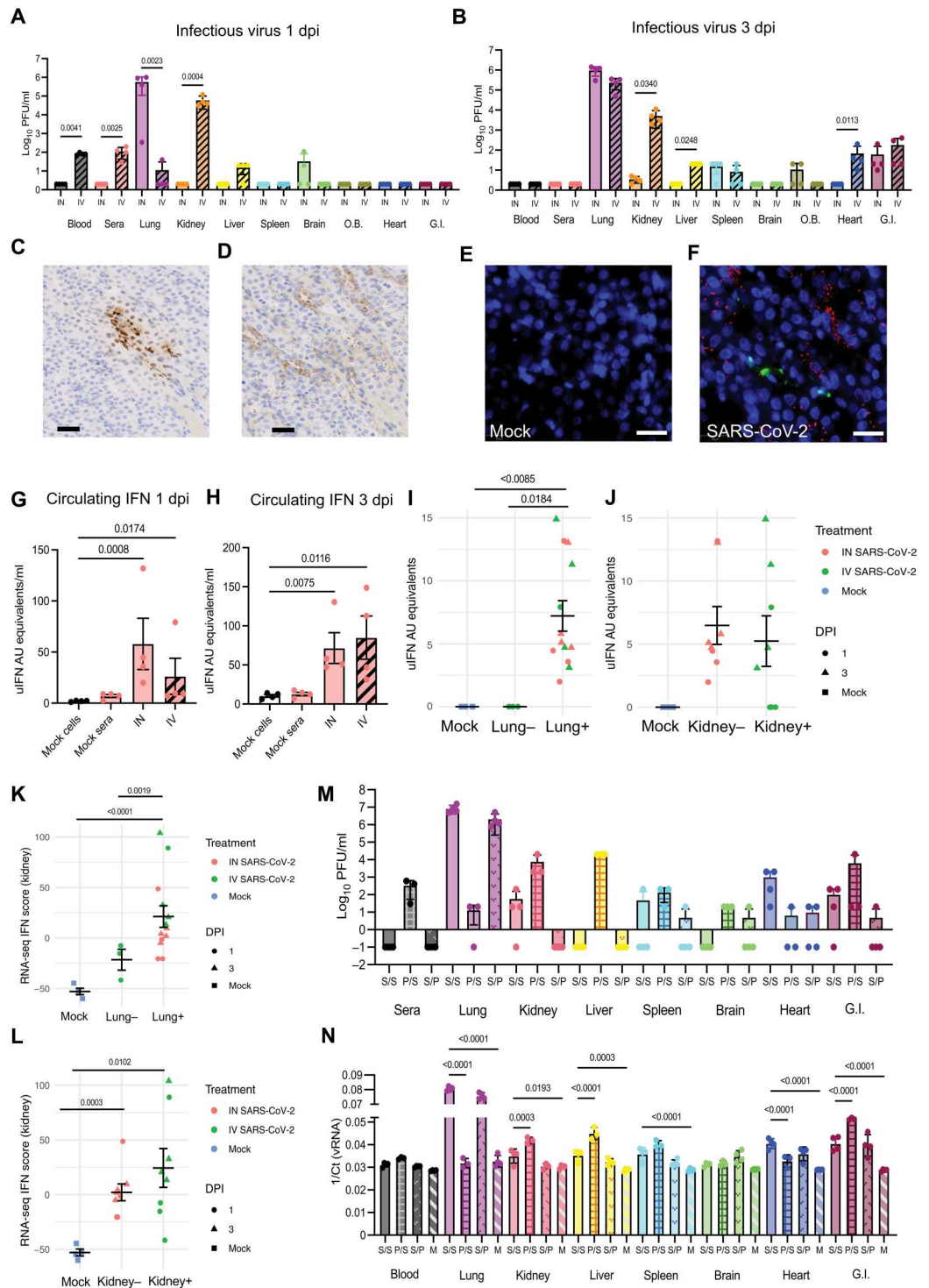
Last, to demonstrate that early circulation of IFN-I/III leads to priming of the organs and protection from infection, we experimentally generated a condition in which we induced the antiviral state and then challenged with virus. We intranasally infected a cohort of animals with SARS-CoV-2, which induces organ priming, and re-challenged the animals at 3 dpi with virus administered intravenously, the route through which more organs are susceptible to productive infection [group S/S denoting SARS-CoV-2 (S) administered intranasally and intravenously]. Organs were harvested at 4 dpi, an early time point that was chosen to measure the impact of the innate antiviral response in the absence of an adaptive immune response, which would take several more days to develop. Control groups included animals intranasally treated with phosphate-buffered saline (PBS) (P), which were challenged 3 days later with SARS-CoV-2 administered intravenously (group P/S), and animals administered SARS-CoV-2 intranasally, which were treated with PBS IV at 3 dpi (group S/P). We reasoned that, if priming protected against infection, then the tissues of animals in the S/S group should be less susceptible to distal infection than tissues of those in the P/S cohort. Consistent with this hypothesis, direct quantification of infectious virus by plaque assay (Fig. 4M) or by RNA levels (Fig. 4N) showed that blood/sera, kidneys, livers, and G.I. tracts from the S/S group showed significantly less virus than those from the P/S group. To assess the level of IFN priming in these organs, we measured *Isg15* expression and found that induction was comparable among all groups, consistent with our findings that engagement in the airways is the major driver of systemic antiviral signaling (fig. S4E).

### DISCUSSION

The hamster model has been extensively used for the study of SARS-CoV-2 infection by our group and others because it phenocopies many aspects of COVID-19, mimicking transmission, clinical presentations, and comorbidities as they relate to disease severity. In this study, we sought to understand the early dynamics between SARS-CoV-2 infection and the innate immune response at a systemic level. Our data suggest that airway exposure to SARS-CoV-2 results in an infection that is largely confined to the upper and lower respiratory tract and, to a lesser extent, the heart while simultaneously inducing a system-wide antiviral response throughout the

**Fig. 4. Lung-derived IFN-I/III protects distal organs from infection. (A and B)**

Viral loads determined by plaque assay in the blood, sera, lungs, kidneys, livers, spleens, brains, O.B.s, hearts, and G.I. tracts of animals intranasally (IN; 1000 PFU) or intravenously (IV;  $1 \times 10^6$  PFU) infected with SARS-CoV-2 at 1 (A) and 3 (B) dpi. Individual dots represent individual animals ( $n = 4$  animals per group per time point). Values are expressed as  $\log_{10}$  PFU/ml. Limit of detection, 20 PFU/ml. Kruskal-Wallis with uncorrected Dunn's test; significant  $P$  values are indicated. (C and D) Representative images of kidneys from golden hamsters IV infected with SARS-CoV-2 ( $1 \times 10^6$  PFU, 3 dpi,  $n = 4$  animals per group). Immunohistochemistry was performed for SARS-CoV-2 nucleocapsid (C) or Mx (D). Scale bars, 50  $\mu$ m. (E and F) Immunofluorescence of representative images of kidneys from golden hamsters mock (E) or intravenously infected with SARS-CoV-2 ( $1 \times 10^6$  PFU, 3 dpi,  $n = 4$  animals per group). Kidney tissue was stained for SARS-CoV-2 N (green), Mx (red), and nucleus DAPI (blue) ( $n = 4$  animals per condition). Scale bar, 20  $\mu$ m. (G and H) Indirect quantification of circulating IFN in sera from animals infected intranasally (1000 PFU) or intravenously ( $1 \times 10^6$  PFU) with SARS-CoV-2 or treated with PBS (mock sera) at 1 (G) and 3 (H) dpi. BHK-21 cells were incubated with the harvest sera for 16 hours, and the induction of Mx was quantified by RT-qPCR analysis. Untreated BHK-21 cells were included as a negative control (mock cells). At each time point, increasing amounts of exogenous uIFN were also included to generate a standard curve. uIFN AU equivalents/ml were calculated by linear regression. (I and J) Correlation plots between mock, presence (+), and absence (-) of infectious virus particles (PFU) in lung (I) or kidney (J) and uIFN (uIFN AU equivalents) in circulation in sera. Error bars represent SD from 4 (mock), 3 (lung-), 13 (lung+), 8 (kidney-), or 8 (kidney+) independent biological replicates per group. One-way ANOVA with Tukey's multiple comparisons test with a single pooled variance; significant  $P$  values are shown. (K and L) Correlation plots between mock, presence (+), and absence (-) of infectious virus particles (PFU) in lung (K) or kidney (L) and the magnitude of the IFN response expressed as RNA-seq IFN score. Error bars represent SD from 4 (mock), 3 (lung-), 13 (lung+), 8 (kidney-), or 8 (kidney+) independent biological replicates per group. Brown-Forsythe and Welch ANOVA with Dunnett's T3 multiple comparisons test, with individual variances computed for each other comparison; significant  $P$  values are shown. (M) Viral loads determined by plaque assay in the sera, lungs, kidneys, livers, spleens, brains, O.B.s, hearts, and G.I. tracts of animals infected as follows: SARS-CoV-2 IN ( $1 \times 10^3$  PFU)/SARS-CoV-2 IV ( $1 \times 10^6$  PFU) (S/S), PBS IN/SARS-CoV-2 IV ( $1 \times 10^6$  PFU) (P/S), or SARS-CoV-2 IN ( $1 \times 10^3$  PFU)/PBS IV (S/P) at 4 days after initial treatment. Individual dots represent individual animals ( $n = 4$  animals per group per time point). Values are expressed as  $\log_{10}$  PFU/ml. Limit of detection, 20 PFU/ml. One animal in



Downloaded from https://www.science.org on February 01, 2024

group P/S was excluded from the analyses because it did not get infected, as indicated by absence of PFU in all tissues, virus RNA (vRNA) levels comparable to mock in all tissues, and no induction of *Isg15* in any organ tested. (N) RT-qPCR analysis for SARS-CoV-2 nucleocapsid (N) gene on RNA extracted from tissues of animals infected as follows: SARS-CoV-2 IN ( $1 \times 10^3$  PFU)/SARS-CoV2 IV ( $1 \times 10^6$  PFU) (S/S), PBS IN/SARS-CoV-2 IV ( $1 \times 10^6$  PFU) (P/S), SARS-CoV-2 IN ( $1 \times 10^3$  PFU)/PBS IV (S/P), or mock-infected at 4 days after initial treatment. Values expressed as 1 over cycle threshold (Ct). Error bars represent SD from four independent biological replicates per group. Brown-Forsythe ANOVA test and unpaired *t* test with Welch's correction with individual variances computed for each comparison; significant *P* values are indicated.

body. Throughout this study, we noted some level of inconsistency related to isolating infectious material in nonpulmonary tissue and believe this to be the product of genetic diversity in outbred hamsters coupled with some level of stochasticity. Despite this heterogeneity, we were able to detect the presence of IFN-I and IFN-III in the sera of all infected animals and found consistency when monitoring the transcriptomes of distal organs, which demonstrated high induction of ISGs such as *Mx1*, *Isg15*, *Oas1*, and *Ifit1-3*, as previously reported elsewhere (14, 15).

To investigate the impact that systemic IFN priming has on SARS-CoV-2 biology, we next sought to explore the consequences of dampening this biological process. Our approach involved the use of the immunosuppressant steroid dexamethasone to delay IFN priming, thus allowing us to assess how this early innate response may affect the outcome of infection. Our results showed that, despite the delay in antiviral signaling, viral titers in the airways remained unchanged, although viral clearance was delayed by 48 to 72 hours compared with the control group. Perhaps more interesting than delayed clearance, our data revealed that virus dissemination occurred more frequently in dexamethasone-treated animals after the initial 24 hours of infection, with liver, spleen, and digestive tract tissues testing positive for SARS-CoV-2. These findings suggest that, in healthy individuals, the initial host response to SARS-CoV-2 in the lungs protects distal organs from subsequent infection. Corroborating this idea, independent groups have reported finding increased viral RNA in distal tissues when IFN-I signaling was genetically disrupted in the hamster model (29).

Considering that COVID-19 often results in more severe symptoms among the elderly population, who also exhibit a diminished immune response (47), our subsequent efforts sought to investigate a possible correlation between SARS-CoV-2 dissemination and the nonpulmonary manifestations associated with severe disease. To this end, we administered SARS-CoV-2 intravenously to bypass the IFN priming event orchestrated by the lung and monitored the behavior of the virus thereafter. These efforts demonstrated that SARS-CoV-2 can productively infect distal organs such as the liver and kidney, corroborating our dexamethasone data and suggesting that IFN priming induced by the lung is essential to containing the virus in the airways.

Overall, our investigation sheds light on the possible mechanisms underlying the nonpulmonary manifestations of severe COVID-19. Here, we propose that, for healthy individuals, this systemic antiviral signaling protects tissues distal to the primary site of infection from the establishment of secondary infections. However, in immune-compromised individuals or those with comorbidities, this same response could result in many of the complications often observed in hospitalized patients with COVID-19. For example, a subset of severe COVID-19 cases are associated with inborn errors of innate immune components and/or autoantibodies against IFN-I that, as the data included here would predict, could result in virus dissemination (46). In addition, the main

comorbidity associated with severe COVID-19 is advanced age, and age delays IFN-I/III responses. The results outlined here make it tempting to speculate that this dynamic could be an underlying driver of some, if not all, of the complications observed after SARS-CoV-2 infection, including the development of Long Covid.

Of the extrapulmonary consequences of COVID-19, kidney-associated diseases or pathologies are some of the most frequent ones in severe cases of COVID-19 (48). In this study, we identified some interesting features in the kidneys of infected animals that could be at the root of some of these complications. Although we could not detect infectious particles in the kidneys of any hamsters infected through the intranasal route, this organ consistently mounted the strongest IFN-I/III signatures upon infection, on occasions even higher than in the lung. If inappropriately regulated, this could then lead to pathological inflammation that could, in turn, affect kidney function. In addition, when virus was introduced directly into the bloodstream, we found that the kidneys were highly susceptible to virus infection, resulting in high titers as early as 1 dpi. Again, the mechanism suggested by the data presented here may represent one of the drivers of kidney-related complications associated with SARS-CoV-2 infection.

This study leveraged hamsters to examine the relationship between SARS-CoV-2 biology and the host response. The findings suggest that, in healthy individuals, the virus is confined to the respiratory tract as a result of a system-wide antiviral response. Should this response be impaired in any way, SARS-CoV-2 can escape the airways and initiate productive infections in distal organs. Although it is tempting to speculate that virus dissemination to nonpulmonary tissues as a result of immune misfiring may underlie the biology of severe clinical cases or even Long Covid, further studies will be needed to further validate this concept.

## MATERIALS AND METHODS

### Cells and viruses

BHK-21 cells and Vero E6 cells (American Type Culture Collection) were maintained in Dulbecco's modified Eagle's medium (DMEM; Gibco) supplemented with 10% fetal bovine serum (FBS) and 1% penicillin/streptomycin. Cells were tested for the presence of mycoplasma using the MycoAlert Mycoplasma Detection Kit (Lonza). SARS-CoV-2 isolate USA-WA1/2020 was propagated in VeroE6 cells grown in DMEM and supplemented with 2% FBS and 1% P/S. The infection was performed at a multiplicity of infection of 0.01 for 48 hours. Supernatants were collected, spun down for 5 min at 2000g, and filtered using an Amicon Ultra-15 Centrifugal filter unit (Sigma-Aldrich). Infectious titers of SARS-CoV-2 were determined by plaque assay on Vero E6 cells with a liquid overlay consisting of DMEM, 4% FBS,  $1 \times$  P/S, and 0.8% agarose. Samples obtained in Fig. 1 were plaqued starting from dilution  $-1$  to  $-6$ . Samples obtained for all other figures were plaqued starting from dilution 0 to  $-5$  to improve sensitivity of the assay. Plaques were fixed after 48 hours in 10% formalin and stained with crystal violet. For

SARS-CoV-2 direct amplification studies, Vero E6 cells were inoculated with 100  $\mu$ l of supernatant from each homogenized hamster tissue sample and incubated at 37°C for 48 hours. Virus titers in cell culture supernatants were quantified by plaque assay on Vero E6 cells.

### In vivo infections

Animal work was performed in accordance with Institutional Animal Care and Use Committee (IACUC) protocols PROTO20210078 and PROTO202000113. Briefly, 5- to 7-week-old male golden Syrian hamsters (*Mesocricetus auratus*) were obtained from the Jackson Laboratory. Hamsters were acclimated to the CDC/United States Department of Agriculture (USDA)-approved biosafety level 3 (BSL-3) facility at the Icahn School of Medicine at Mount Sinai or the CDC/USDA-approved BSL-3 facility at the Grossman School of Medicine at NYU Langone. Animals were maintained in a 12-hour light/dark cycle, housed in pairs in airtight cages, and fed ad libitum with PicoLab Rodent Diet 20 5053. Under ketamine:xylazine (4:1) anesthesia, hamsters were infected intranasally with PBS (mock) or 1000 PFU of SARS-CoV-2 diluted in 100  $\mu$ l of PBS or intravenously in the retroorbital venous plexus with  $1 \times 10^6$  PFU in 100  $\mu$ l. Dexamethasone was prepared fresh each day before administration at a dose of 1 mg/kg in 0.5 ml of 20% dimethyl sulfoxide/60% polyethylene glycol 400 (PEG400)/20% 2-hydroxypropyl- $\beta$ -cyclodextrin in water (w/w) and administered by subcutaneous injection. At selected time points, animals were anesthetized intraperitoneally with pentobarbital:PBS (1:4) and cervically dislocated. Blood was collected in tubes containing heparin, and organs were collected in 1 ml of PBS and/or TRIzol Reagent (Invitrogen). Tissues were homogenized in a TissueLyser machine (Qiagen) for two cycles of  $2 \times 40$  s, then samples were centrifuged for 5 min at 5000g and supernatants containing virus were collected and stored at  $-80^\circ\text{C}$  for virus titration or RNA extraction.

### Tissue histology

Upon euthanization of animals, tissues were harvested into 4% paraformaldehyde (PFA) for 48 hours at room temperature, at which time PFA was replaced by 70% ethanol and tissues were stored at 4°C. Tissues were embedded in paraffin and sectioned onto slides by the microscopy core at NYU Langone. For immunohistochemistry, SARS-CoV-2 N protein was detected using mouse monoclonal anti-SARS-CoV-2 N (1C7C7) (gifted by T. Moran, Center for Therapeutic Antibody Discovery at the Icahn School of Medicine at Mount Sinai). Mx staining was performed with the anti-MxA clone M143 (CL143), a mouse monoclonal antibody (EMD Millipore, MABF938). For protein quantification from immunohistochemistry, five representative sections of each tissue were selected and blindly quantified using Particle Analysis in ImageJ v2.1/1.53c. For immunofluorescence, tissues were stained with 1C7C7 at a 1:50 dilution. IBA1 staining was performed with an anti-IBA1 antibody from FUJIFILM Wako (catalog no. 019-19741). Tissue sections were acquired using a fluorescent microscope, and quantifications were made by automated cell count using Particle Analysis in ImageJ v2.1/1.53c. Images were taken by an investigator blinded to treatment conditions using identical acquisition parameters. IBA1-positive cells were counted over the entire lung using a 20 $\times$  objective and then expressed as cells per unit area. To count IBA1-positive cells, the threshold for 4',6-

diamidino-2-phenylindole-stained nuclei was merged with the IBA1 threshold, and the number of overlapped objects therefore represents the positive cell number.

### Serum incubation experiments

At 1 or 3 days after SARS-CoV-2 infection or PBS treatment of hamsters, whole blood was collected in BD Microtainer blood collection tubes on ice, and serum was separated by centrifugation for 5 min at 7000g. Serum was directly added to BHK-21 cells at different doses in equal total volumes of BHK-21 growth medium. Cells and sera were incubated together for 16 hours at 37°C. After incubation, cells were harvested in TRIzol Reagent for RNA extraction and RT-qPCR, as described below.

### RNA extraction and quantification

Total RNA from hamster samples was isolated using TRIzol Reagent (Invitrogen) and following the manufacturer's recommendations. RNA was deoxyribonuclease (DNase)-treated and purified using RNA Clean & Concentrator (Zymo Research). RNA samples were quantified using a NanoDrop spectrophotometer and diluted to a concentration of 100 ng/ $\mu$ l. RT-qPCR was performed using primers specific for each gene of interest (data file S5) with the Luna Universal One-Step RT-qPCR kit (New England Biolabs) for SYBR green chemistry and Luna Universal Probe One-Step RT-qPCR (New England Biolabs) for Taqman chemistry. In either case, the reaction mix contained 100 ng of RNA, 500 nM each primer, 1  $\mu$ l of RT enzyme, 2 $\times$  reaction mix, 0.25 M betaine, 20  $\mu$ g of bovine serum albumin, ribonuclease (RNase)-free water, and 120 nM probe for Taqman assays in 10  $\mu$ l of final volume. Reactions were run on a LightCycler 480 Instrument II (Roche) or in a Quantstudio 6 Real Time PCR system (Applied Biosystems) using amplification conditions recommended by each RT-qPCR kit. The  $\Delta\Delta$  Cycle threshold ( $\Delta\Delta\text{Ct}$ ) was determined relative to mock-infected control for SYBR green reactions.

### RNA sequencing

RNA-seq libraries of polyadenylated RNA extracted from selected tissues were prepared using the TruSeq RNA Library Prep Kit v2 (Illumina) according to the manufacturer's instructions. The libraries were sequenced on an Illumina NextSeq 500 instrument.

### SARS-CoV-2 RPM analyses

To calculate reads per million (RPM) of SARS-CoV-2 RNA, total Illumina RNA-seq libraries were aligned to the *M. auratus* genome (MesAur1.0) and the SARS-CoV-2 genome (GenBank, MN985325.1) using Bowtie2. Total aligned reads for SARS-CoV-2 were divided by total reads divided by 1 M to generate a qualitative and quantitative measure of virus RNA levels.

### Ifnb and Ifnl RPM analyses

To calculate RPM of *Ifnb* or *Ifnl* RNA, total Illumina RNA-seq libraries were aligned to the *M. auratus* genome (MesAur1.0) using Bowtie2. Total aligned reads for each gene were divided by total reads and normalized for 100 million to generate a qualitative and quantitative measure of gene RNA levels.

### Differential gene expression analyses

Raw reads were aligned to the *M. auratus* genome (MesAur1.0) using the RNA-Seq Alignment App on Basespace (Illumina, CA),

followed by differential expression analysis using DESeq2<sup>26</sup>, by matching each experimental condition with corresponding mock-infected samples of the same nature (tissue, day after infection, cell type, etc.). DEGs were characterized for each sample ( $\log_2$  fold change  $> 2$ ,  $P$ -adjusted value  $< 0.05$ ) and were used as a query to search for enriched Hallmark gene sets (49, 50) using Enrichr (51–53). Heatmaps of DEGs belonging to the Hallmark IFN- $\alpha$  response gene set were constructed using heatmap.2 from the gplot package in R (<https://cran.r-project.org/web/packages/gplots/index.html>). Dot plots of enriched Hallmark gene sets were constructed using ggplot2 (<https://ggplot2.tidyverse.org/>) and custom scripts in R. Alignments to the SARS-CoV-2 genome (GenBank, MN985325.1) were performed using Bowtie2 (54).

### RNA-seq IFN score stratification

To assess how transcriptomic IFN responses correlated with cohort metadata,  $z$  scores were calculated for each gene available in transcriptomic analyses. Gene  $z$  scores were calculated across each harvested organ type from normalized read counts of mock, intravenously, and intranasally infected samples at 1 and 3 dpi. Total “RNA-seq IFN score” was calculated for a given sample by summing  $z$  scores of all genes present in a set of ISGs adapted from the MSigDB “HALLMARK\_INTERFERON\_ALPHA\_RESPONSE” geneset.

### Flow cytometry

The methods used for flow cytometry were described previously (42). In brief, lungs were collected upon perfusion with 30 ml of PBS to avoid contamination of lymphocytes from the blood. After collection, lungs were dissociated by Miltenyi GentleMACS using the lung dissociation kit protocol and after incubation in 37°C for 30 min with 2 ml of collagenase (1 mg/ml) and DNase (0.5 mg/ml) in RPMI medium. Dissociated lung cells were then extracellularly stained with anti-MHC class II (14-4-4 s; Thermo Fisher Scientific) at room temperature. For intracellular staining, cells were fixed for 30 min at 4°C with Fix Buffer I (BD Biosciences) and then incubated overnight at 4°C with anti-CD3 (CD3-12; BioRad) in Perm/Wash Buffer (BD Biosciences). Total T cells were defined as CD3<sup>+</sup>/MHCII<sup>-</sup>, and total B cells were defined as CD3<sup>-</sup>/MHCII<sup>+</sup>. To exclude dead cells, all samples were labeled with LIVE/DEAD Fixable Yellow (Invitrogen). Antibody-stained cells were acquired on an Attune Flow Cytometer (Thermo Fisher Scientific), and the expression of each molecule was assessed with FlowJo software (TreeStar).

### Data visualization

All non-RNA-seq statistical analyses and box and bar graphs were performed as indicated in the figure legends, using Prism 8 (GraphPad Software, San Diego, CA, USA; [www.graphpad.com/](http://www.graphpad.com/)).

### Supplementary Materials

This PDF file includes:

Figs. S1 to S4

Other Supplementary Material for this manuscript includes the following:

Data files S1 to S5

MDAR Reproducibility Checklist

[View/request a protocol for this paper from Bio-protocol.](#)

### REFERENCES AND NOTES

1. Y. J. Hou, K. Okuda, C. E. Edwards, D. R. Martinez, T. Asakura, K. H. Dinnon III, T. Kato, R. E. Lee, B. L. Yount, T. M. Mascenik, G. Chen, K. N. Olivier, A. Ghio, L. V. Tse, S. R. Leist, L. E. Gralinski, A. Schäfer, H. Dang, R. Gilmore, S. Nakano, L. Sun, M. L. Fulcher, A. Livraghi-Butrico, N. I. Nicely, M. Cameron, C. Cameron, D. J. Kelvin, A. de Silva, D. M. Margolis, A. Markmann, L. Bartelt, R. Zumwalt, F. J. Martinez, S. P. Salvatore, A. Borczuk, P. R. Tata, V. Sontake, A. Kimple, I. Jaspers, W. K. O’Neal, S. H. Randell, R. C. Boucher, R. S. Baric, SARS-CoV-2 reverse genetics reveals a variable infection gradient in the respiratory tract. *Cell* **182**, 429–446.e14 (2020).
2. P. V’Kovski, A. Kratzel, S. Steiner, H. Stalder, V. Thiel, Coronavirus biology and replication: Implications for SARS-CoV-2. *Nat. Rev. Microbiol.* **19**, 155–170 (2021).
3. A. Sariol, S. Perlman, SARS-CoV-2 takes its Toll. *Nat. Immunol.* **22**, 801–802 (2021).
4. Y. Li, D. M. Renner, C. E. Comar, J. N. Whelan, H. M. Reyes, F. L. Cardenas-Diaz, R. Truitt, L. H. Tan, B. Dong, K. D. Alysandratos, J. Huang, J. N. Palmer, N. D. Adappa, M. A. Kohanski, D. N. Kotton, R. H. Silverman, W. Yang, E. E. Morrissy, N. A. Cohen, S. R. Weiss, SARS-CoV-2 induces double-stranded RNA-mediated innate immune responses in respiratory epithelial-derived cells and cardiomyocytes. *Proc. Natl. Acad. Sci. U.S.A.* **118**, (2021).
5. B. E. Nilsson-Payant, S. Uhl, A. Grimont, A. S. Doane, P. Cohen, R. S. Patel, C. A. Higgins, J. A. Acklin, Y. Bram, V. Chandar, D. Blanco-Melo, M. Panis, J. K. Lim, O. Elemento, R. E. Schwartz, B. R. Rosenberg, R. Chandwani, B. R. tenOever, The NF- $\kappa$ B transcriptional footprint is essential for SARS-CoV-2 replication. *J. Virol.* **95**, (2021).
6. D. Blanco-Melo, B. E. Nilsson-Payant, W. C. Liu, S. Uhl, D. Hoagland, R. Möller, T. X. Jordan, K. Oishi, M. Panis, D. Sachs, T. T. Wang, R. E. Schwartz, J. K. Lim, R. A. Albrecht, B. R. tenOever, Imbalanced host response to SARS-CoV-2 drives development of COVID-19. *Cell* **181**, 1036–1045.e9 (2020).
7. T. S. Rodrigues, K. S. G. de Sá, A. Y. Ishimoto, A. Becerra, S. Oliveira, L. Almeida, A. V. Gonçalves, D. B. Perucello, W. A. Andrade, R. Castro, F. P. Veras, J. E. Toller-Kawahisa, D. C. Nascimento, M. H. F. de Lima, C. M. S. Silva, D. B. Caetite, R. B. Martins, I. A. Castro, M. C. Pontelli, F. C. de Barros, N. B. do Amaral, M. C. Giannini, L. P. Bonjorno, M. I. F. Lopes, F. R. C. Santana, F. C. Vilar, M. Auxiliadora-Martins, R. Luppino-Assad, S. C. L. de Almeida, F. R. de Oliveira, S. S. Batah, L. Siyuan, M. N. Benatti, T. M. Cunha, J. C. Alves-Filho, F. Q. Cunha, L. D. Cunha, F. G. Frantz, T. Kohlsdorf, A. T. Fabro, E. Arruda, R. D. R. de Oliveira, P. Louzada-Junior, D. S. Zamboni, Inflammasomes are activated in response to SARS-CoV-2 infection and are associated with COVID-19 severity in patients. *J. Exp. Med.* **218**, (2021).
8. S. Li, Y. Zhang, Z. Guan, H. Li, M. Ye, X. Chen, J. Shen, Y. Zhou, Z. L. Shi, P. Zhou, K. Peng, SARS-CoV-2 triggers inflammatory responses and cell death through caspase-8 activation. *Signal Transduct. Target. Ther.* **5**, 235 (2020).
9. J. W. Schoggins, Interferon-stimulated genes: What do they all do? *Annu. Rev. Virol.* **6**, 567–584 (2019).
10. C. Lucas, P. Wong, J. Klein, T. B. R. Castro, J. Silva, M. Sundaram, M. K. Ellingson, T. Mao, J. E. Oh, B. Israelow, T. Takahashi, M. Tokuyama, P. Lu, A. Venkataraman, A. Park, S. Mohanty, H. Wang, A. L. Wyllie, C. B. F. Vogels, R. Earnest, S. Lapidus, I. M. Ott, A. J. Moore, M. C. Muenker, J. B. Fournier, M. Campbell, C. D. Odio, A. Casanovas-Massana; Yale IMPACT Team, A. Obaid, A. Lu-Culligan, A. Nelson, A. Brito, A. Nunez, A. Martin, A. Watkins, B. Geng, C. Kalinich, C. Harden, C. Todeasa, C. Jensen, D. Kim, D. McDonald, D. Shepard, E. Courchaine, E. B. White, E. Song, E. Silva, E. Kudo, G. Deluiliis, H. Rahming, H. J. Park, I. Matos, J. Nouws, J. Valdez, J. Fauver, J. Lim, K. A. Rose, K. Anastasio, K. Brower, L. Glick, L. Sharma, L. Swanan, L. Knaggs, M. Minasyan, M. Batsu, M. Petrone, M. Kuang, M. Nakahata, M. Campbell, M. Linehan, M. H. Askenase, M. Simonov, M. Smolgovsky, N. Sonner, N. Naushad, P. Vijayakumar, R. Martinello, R. Datta, R. Handoko, S. Bermejo, S. Prophet, S. Bickerton, S. Velazquez, T. Alpert, T. Rice, W. Khoury-Hanold, X. Peng, Y. Yang, Y. Cao, Y. Strong, R. Herbst, A. C. Shaw, R. Medzhitov, W. L. Schulz, N. D. Grubaugh, C. dela Cruz, S. Farhadian, A. I. Ko, S. B. Omer, A. Iwasaki, Longitudinal analyses reveal immunological misfiring in severe COVID-19. *Nature* **584**, 463–469 (2020).
11. F. P. Veras, M. C. Pontelli, C. M. Silva, J. E. Toller-Kawahisa, M. de Lima, D. C. Nascimento, A. H. Schneider, D. Caetite, L. A. Tavares, I. M. Paiva, R. Rosales, D. Colón, R. Martins, I. A. Castro, G. M. Almeida, M. I. F. Lopes, M. N. Benatti, L. P. Bonjorno, M. C. Giannini, R. Luppino-Assad, S. L. Almeida, F. Vilar, R. Santana, V. R. Bollela, M. Auxiliadora-Martins, M. Borges, C. H. Miranda, A. Pazin-Filho, L. L. P. da Silva, L. D. Cunha, D. S. Zamboni, F. Dal-Pizzol, L. O. Leiria, L. Siyuan, S. Batah, A. Fabro, T. Mauad, M. Dolnikoff, A. Duarte-Neto, P. Saldiva, T. M. Cunha, J. C. Alves-Filho, E. Arruda, P. Louzada-Junior, R. D. Oliveira, F. Q. Cunha, SARS-CoV-2-triggered neutrophil extracellular traps mediate COVID-19 pathology. *J. Exp. Med.* **217**, (2020).
12. B. K. Manne, F. Denorme, E. A. Middleton, I. Portier, J. W. Rowley, C. Stubben, A. C. Petrey, N. D. Tolley, L. Guo, M. Cody, A. S. Weyrich, C. C. Yost, M. T. Rondina, R. A. Campbell, Platelet gene expression and function in patients with COVID-19. *Blood* **136**, 1317–1329 (2020).

13. V. J. Munster, F. Feldmann, B. N. Williamson, N. van Doremalen, L. Pérez-Pérez, J. Schulz, K. Meade-White, A. Okumura, J. Callison, B. Brumbaugh, V. A. Avanzato, R. Rosenke, P. W. Hanley, G. Saturday, D. Scott, E. R. Fischer, E. de Wit, Respiratory disease in rhesus macaques inoculated with SARS-CoV-2. *Nature* **585**, 268–272 (2020).
14. D. A. Hoagland, R. Möller, S. A. Uhl, K. Oishi, J. Frere, I. Golynger, S. Horiuchi, M. Panis, D. Blanco-Melo, D. Sachs, K. Arkun, J. K. Lim, B. R. tenOever, Leveraging the antiviral type I interferon system as a first line of defense against SARS-CoV-2 pathogenicity. *Immunity* **54**, 557–570.e5 (2021).
15. J. J. Frere, R. A. Serafini, K. D. Pryce, M. Zazhytska, K. Oishi, I. Golynger, M. Panis, J. Zimering, S. Horiuchi, D. A. Hoagland, R. Möller, A. Ruiz, A. Kodra, J. B. Overdevest, P. D. Canoll, A. C. Borczuk, V. Chandar, Y. Bram, R. Schwartz, S. Lomvardas, V. Zachariou, B. R. tenOever, SARS-CoV-2 infection in hamsters and humans results in lasting and unique systemic perturbations after recovery. *Sci. Transl. Med.* **14**, (2022).
16. A. G. Laing, A. Lorenc, I. del Molino del Barrio, A. das, M. Fish, L. Monin, M. Muñoz-Ruiz, D. R. McKenzie, T. S. Hayday, I. Francos-Quijorna, S. Kamdar, M. Joseph, D. Davies, R. Davis, A. Jennings, I. Zlatareva, P. Vantourout, Y. Wu, V. Sofra, F. Cano, M. Greco, E. Theodoridis, J. D. Freedman, S. Gee, J. N. E. Chan, S. Ryan, E. Bugallo-Blanco, P. Peterson, K. Kisand, L. Haljasmägi, L. Chadli, P. Moingeon, L. Martinez, B. Merrick, K. Bisnauthsing, K. Brooks, M. A. A. Ibrahim, J. Mason, F. Lopez Gomez, K. Babalola, S. Abdul-Jawad, J. Cason, C. Mant, J. Seow, C. Graham, K. J. Doores, F. di Rosa, J. Edgeworth, M. Shankar-Hari, A. C. Hayday, A dynamic COVID-19 immune signature includes associations with poor prognosis. *Nat. Med.* **26**, 1623–1635 (2020).
17. N. Desai, A. Neyaz, A. Szabolcs, A. R. Shih, J. H. Chen, V. Thapar, L. T. Nieman, A. Solovyov, A. Mehta, D. J. Lieb, A. S. Kulkarni, C. Jaicks, K. H. Xu, M. J. Raabe, C. J. Pinto, D. Juric, I. Chebib, R. B. Colvin, A. Y. Kim, R. Monroe, S. E. Warren, P. Danaher, J. W. Reeves, J. Gong, E. H. Rueckert, B. D. Greenbaum, N. Hacohen, S. M. Lagana, M. N. Rivera, L. M. Sholl, J. R. Stone, D. T. Ting, V. Deshpande, Temporal and spatial heterogeneity of host response to SARS-CoV-2 pulmonary infection. *Nat. Commun.* **11**, 6319 (2020).
18. A. Gupta, M. V. Madhavan, K. Sehgal, N. Nair, S. Mahajan, T. S. Sehrawat, B. Bikkdeli, N. Ahluwalia, J. C. Ausiello, E. Y. Wan, D. E. Freedberg, A. J. Kirtane, S. A. Parikh, M. S. Maurer, A. S. Nordvig, D. Accili, J. M. Bathon, S. Mohan, K. A. Bauer, M. B. Leon, H. M. Krumholz, N. Uriel, M. R. Mehra, M. S. V. Elkind, G. W. Stone, A. Schwartz, D. D. Ho, J. P. Bilezikian, D. W. Landry, Extrapulmonary manifestations of COVID-19. *Nat. Med.* **26**, 1017–1032 (2020).
19. M. O'Driscoll, G. Ribeiro Dos Santos, L. Wang, D. A. T. Cummings, A. S. Azman, J. Paireau, A. Fontanet, S. Cauchemez, H. Salje, Age-specific mortality and immunity patterns of SARS-CoV-2. *Nature* **590**, 140–145 (2021).
20. J. Yang, Y. Zheng, X. Gou, K. Pu, Z. Chen, Q. Guo, R. Ji, H. Wang, Y. Wang, Y. Zhou, Prevalence of comorbidities and its effects in patients infected with SARS-CoV-2: A systematic review and meta-analysis. *Int. J. Infect. Dis.* **94**, 91–95 (2020).
21. F. Braun, M. Lütgehetmann, S. Pfeifferle, M. N. Wong, A. Carsten, M. T. Lindenmeyer, D. Nörz, F. Heinrich, K. Meißner, D. Wichmann, S. Kluge, O. Gross, K. Püschel, A. S. Schröder, C. Edler, M. Aepfelbacher, V. G. Puelles, T. B. Huber, SARS-CoV-2 renal tropism associates with acute kidney injury. *Lancet* **396**, 597–598 (2020).
22. T. Solomon, Neurological infection with SARS-CoV-2 - the story so far. *Nat. Rev. Neurol.* **17**, 65–66 (2021).
23. S. Deinhardt-Emmer, D. Wittschieber, J. Sanft, S. Kleemann, S. Elschner, K. F. Haupt, V. Vau, C. Häring, J. Rödel, A. Henke, C. Ehrhardt, M. Bauer, M. Philipp, N. Gäßler, S. Nietzsche, B. Löffler, G. Mall, Early postmortem mapping of SARS-CoV-2 RNA in patients with COVID-19 and the correlation with tissue damage. *eLife* **10**, (2021).
24. C. C. L. Cheung, D. Goh, X. Lim, T. Z. Tien, J. C. T. Lim, J. N. Lee, B. Tan, Z. E. A. Tay, W. Y. Wan, E. X. Chen, S. N. Nerurkar, S. Loong, P. C. Cheow, C. Y. Chan, Y. X. Koh, T. T. Tan, S. Kalimuddin, W. M. D. Tai, J. L. Ng, J. G. H. Low, J. Yeong, K. H. Lim, Residual SARS-CoV-2 viral antigens detected in GI and hepatic tissues from five recovered patients with COVID-19. *Gut* **71**, 226–229 (2022).
25. J. Van Cleemput, W. van Snippenberg, L. Lambrechts, A. Dendooven, V. D'Onofrio, L. Couck, W. Trypsteen, J. Vanrusselt, S. Theuns, N. Vereecke, T. P. P. van den Bosch, M. Lammens, A. Driessen, R. Achten, K. R. Bracke, W. Van den Broeck, J. Von der Thüsen, H. Nauwynck, J. Van Dorpe, S. Gerlo, P. Maes, J. Cox, L. Vandekerckhove, Organ-specific genome diversity of replication-competent SARS-CoV-2. *Nat. Commun.* **12**, 6612 (2021).
26. M. Imai, K. Iwatsuki-Horimoto, M. Hatta, S. Loeber, P. J. Halfmann, N. Nakajima, T. Watanabe, M. Ujie, K. Takahashi, M. Ito, S. Yamada, S. Fan, S. Chiba, M. Kuroda, L. Guan, K. Takada, T. Armbrust, A. Balogh, Y. Furusawa, M. Okuda, H. Ueki, A. Yasuhara, Y. Sakai-Tagawa, T. J. S. Lopes, M. Kiso, S. Yamayoshi, N. Kinoshita, N. Ohmagari, S. I. Hattori, M. Takeda, H. Mitsuya, F. Krammer, T. Suzuki, Y. Kawaoka, Syrian hamsters as a small animal model for SARS-CoV-2 infection and countermeasure development. *Proc. Natl. Acad. Sci. U.S.A.* **117**, 16587–16595 (2020).
27. K. Rosenke, K. Meade-White, M. Letko, C. Clancy, F. Hansen, Y. Liu, A. Okumura, T. L. Tang-Huau, R. Li, G. Saturday, F. Feldmann, D. Scott, Z. Wang, V. Munster, M. A. Jarvis, H. Feldmann, Defining the Syrian hamster as a highly susceptible preclinical model for SARS-CoV-2 infection. *Emerg. Microbes Infect.* **9**, 2673–2684 (2020).
28. N. Osterrieder, L. D. Bertzbach, K. Diertert, A. Abdelgawad, D. Vladimirova, D. Kunec, D. Hoffmann, M. Beer, A. D. Gruber, J. Trimpert, Age-dependent progression of SARS-CoV-2 infection in Syrian hamsters. *Viruses* **12**, (2020).
29. R. Boudewijns, H. J. Thibaut, S. J. F. Kaptein, R. Li, V. Vergote, L. Seldeslachts, J. van Weyenbergh, C. de Kuyzer, L. Bervoets, S. Sharma, L. Liesenborghs, J. Ma, S. Jansen, D. van Looveren, T. Vercauysse, X. Wang, D. Jochmans, E. Martens, K. Roose, D. de Vlieger, B. Schepens, T. van Buyten, S. Jacobs, Y. Liu, J. Martí-Carreras, B. Vanmechelen, T. Wawina-Bokalanga, L. Delang, J. Rocha-Pereira, L. Coelmont, W. Chiu, P. Leyssen, E. Heylen, D. Schols, L. Wang, L. Close, J. Matthijssens, M. van Ranst, V. Compennolle, G. Schramm, K. van Laere, X. Saelens, N. Callewaert, G. Opendakker, P. Maes, B. Weynand, C. Cawthorne, G. Vande Velde, Z. Wang, J. Neyts, K. Dallmeier, STAT2 signaling restricts viral dissemination but drives severe pneumonia in SARS-CoV-2 infected hamsters. *Nat. Commun.* **11**, 5838 (2020).
30. K. Oishi, S. Horiuchi, J. M. Minkoff, B. R. tenOever, The host response to influenza A virus interferes with SARS-CoV-2 replication during coinfection. *J. Virol.* **96**, e0076522 (2022).
31. A. K. Nalla, A. M. Casto, M. L. W. Huang, G. A. Perchetti, R. Sampoleo, L. Shrestha, Y. Wei, H. Zhu, K. R. Jerome, A. L. Greninger, Comparative performance of SARS-CoV-2 detection assays using seven different primer-probe sets and one assay kit. *J. Clin. Microbiol.* **58**, (2020).
32. S. Schmid, M. Mordstein, G. Kochs, A. Garcia-Sastre, B. R. Tenover, Transcription factor redundancy ensures induction of the antiviral state. *J. Biol. Chem.* **285**, 42013–42022 (2010).
33. X. Yin, L. Riva, Y. Pu, L. Martin-Sancho, J. Kanamune, Y. Yamamoto, K. Sakai, S. Gotoh, L. Miorin, P. D. de Jesus, C. C. Yang, K. M. Herbert, S. Yoh, J. F. Hultquist, A. Garcia-Sastre, S. K. Chanda, MDA5 governs the innate immune response to SARS-CoV-2 in lung epithelial cells. *Cell Rep.* **34**, 108628 (2021).
34. T. Agaloti, S. Lomvardas, B. Parekh, J. Yie, T. Maniatis, D. Thanos, Ordered recruitment of chromatin modifying and general transcription factors to the IFN-beta promoter. *Cell* **103**, 667–678 (2000).
35. K. Oishi, S. Horiuchi, J. Frere, R. E. Schwartz, B. R. tenOever, A diminished immune response underlies age-related SARS-CoV-2 pathologies. *Cell Rep.* **39**, 111002 (2022).
36. C. H. Woelk, S. D. Frost, D. D. Richman, P. E. Higley, S. L. Kosakovsky Pond, Evolution of the interferon alpha gene family in eutherian mammals. *Gene* **397**, 38–50 (2007).
37. K. Otsuki, J. Maeda, H. Yamamoto, M. Tsubokura, Studies on avian infectious bronchitis virus (IBV). III. Interferon induction by and sensitivity to interferon of IBV. *Arch. Virol.* **60**, 249–255 (1979).
38. Q. Zhang, P. Bastard, C. H. G. Effort, A. Cobat, J. L. Casanova, Human genetic and immunological determinants of critical COVID-19 pneumonia. *Nature* **603**, 587–598 (2022).
39. B. J. Thomas, R. A. Porritt, P. J. Hertzog, P. G. Bardin, M. D. Tate, Glucocorticosteroids enhance replication of respiratory viruses: Effect of adjuvant interferon. *Sci. Rep.* **4**, 7176 (2014).
40. L. Yang, Y. Han, B. E. Nilsson-Payant, V. Gupta, P. Wang, X. Duan, X. Tang, J. Zhu, Z. Zhao, F. Jaffré, T. Zhang, T. W. Kim, O. Harschnitz, D. Redmond, S. Houghton, C. Liu, A. Naji, G. Ciceri, S. Guttikonda, Y. Bram, D. H. T. Nguyen, M. Cioffi, V. Chandar, D. A. Hoagland, Y. Huang, J. Xiang, H. Wang, D. Lyden, A. Borczuk, H. J. Chen, L. Studer, F. C. Pan, D. D. Ho, B. R. tenOever, T. Evans, R. E. Schwartz, S. Chen, A human pluripotent stem cell-based platform to study SARS-CoV-2 tropism and model virus infection in human cells and organoids. *Cell Stem Cell* **27**, 125–136.e7 (2020).
41. Y. Han, X. Duan, L. Yang, B. E. Nilsson-Payant, P. Wang, F. Duan, X. Tang, T. M. Yaron, T. Zhang, S. Uhl, Y. Bram, C. Richardson, J. Zhu, Z. Zhao, D. Redmond, S. Houghton, D. H. T. Nguyen, D. Xu, X. Wang, J. Jessurun, A. Borczuk, Y. Huang, J. L. Johnson, Y. Liu, J. Xiang, H. Wang, L. C. Cantley, B. R. tenOever, D. D. Ho, F. C. Pan, T. Evans, H. J. Chen, R. E. Schwartz, S. Chen, Identification of SARS-CoV-2 inhibitors using lung and colonic organoids. *Nature* **589**, 270–275 (2021).
42. S. Horiuchi, K. Oishi, L. Carrau, J. Frere, R. Möller, M. Panis, B. R. tenOever, Immune memory from SARS-CoV-2 infection in hamsters provides variant-independent protection but still allows virus transmission. *Sci. Immunol.* **6**, eabm3131 (2021).
43. The Immunological Genome Project, ImmGen at 15. *Nat. Immunol.* **21**, 700–703 (2020).
44. B. Choi, M. C. Choudhary, J. Regan, J. A. Sparks, R. F. Padera, X. Qiu, I. H. Solomon, H. H. Kuo, J. Boucau, K. Bowman, U. D. Adhikari, M. L. Winkler, A. A. Mueller, T. Y. T. Hsu, M. Desjardins, L. R. Baden, B. T. Chan, B. D. Walker, M. Lichterfeld, M. Brigl, D. S. Kwon, S. Kanjilal, E. T. Richardson, A. H. Jonsson, G. Alter, A. K. Barczak, W. P. Hanage, X. G. Yu, G. D. Gaiha, M. S. Seaman, M. Cernadas, J. Z. Li, Persistence and evolution of SARS-CoV-2 in an immunocompromised host. *N. Engl. J. Med.* **383**, 2291–2293 (2020).
45. N. S. Ogando, T. J. Dalebout, J. C. Zevenhoven-Dobbe, R. W. A. L. Limpens, Y. van der Meer, L. Cally, J. Druce, J. J. C. de Vries, M. Kikkert, M. Bärkena, I. Sidorov, E. J. Snijder, SARS-coronavirus-2 replication in Vero E6 cells: Replication kinetics, rapid adaptation and cytopathology. *J. Gen. Virol.* **101**, 925–940 (2020).

46. P. Bastard, L. B. Rosen, Q. Zhang, E. Michailidis, H. H. Hoffmann, Y. Zhang, K. Dorgham, Q. Philippot, J. Rosain, V. Béziat, J. Manry, E. Shaw, L. Haljasmägi, P. Peterson, L. Lorenzo, L. Bizien, S. Trouillet-Assant, K. Dobbs, A. A. de Jesus, A. Belot, A. Kallaste, E. Catherinot, Y. Tandjaoui-Lambiotte, J. Le Pen, G. Kerner, B. Bigio, Y. Seeleuthner, R. Yang, A. Bolze, A. N. Spaan, O. M. Delmonte, M. S. Abers, A. Aiuti, G. Casari, V. Lampasona, L. Piemonti, F. Ciceri, K. Bilguvar, R. P. Lifton, M. Vasse, D. M. Smadja, M. Migaud, J. Hadjadj, B. Terrier, D. Duffy, L. Quintana-Murci, D. van de Beek, L. Rousset, D. C. Vinh, S. G. Tangye, F. Haerynck, D. Dalmau, J. Martinez-Picado, P. Brodin, M. C. Nussenzweig, S. Boisson-Dupuis, C. Rodriguez-Gallego, G. Vogt, T. H. Mogensen, A. J. Oler, J. Gu, P. D. Burbelo, J. I. Cohen, A. Biondi, L. R. Bettini, M. D'Angio, P. Bonfanti, P. Rossignol, J. Mayaux, F. Rieux-Laucat, E. S. Husebye, F. Fusco, M. V. Ursini, L. Imberti, A. Sottini, S. Paghera, E. Quiros-Roldan, C. Rossi, R. Castagnoli, D. Montagna, A. Licari, G. L. Marseglia, X. Duval, J. Ghosn; HGID Lab; NIAID-USUHS Immune Response to COVID Group; COVID Clinicians; COVID-STORM Clinicians; Imagine COVID Group; French COVID Cohort Study Group; The Milieu Intérieur Consortium; CoV-Contact Cohort; Amsterdam UMC Covid-19 Biobank; COVID Human Genetic Effort, J. S. Tsang, R. Goldbach-Mansky, K. Kisand, M. S. Lionakis, A. Puel, S. Y. Zhang, S. M. Holland, G. Gorochov, E. Jouanguy, C. M. Rice, A. Cobat, L. D. Notarangelo, L. Abel, H. C. Su, J. L. Casanova, Autoantibodies against type I IFNs in patients with life-threatening COVID-19. *Science* **370**, eabd4585 (2020).
47. J. M. Bartleson, D. Radenkovic, A. J. Covarrubias, D. Furman, D. A. Winer, E. Verdin, SARS-CoV-2, COVID-19 and the ageing immune system. *Nat. Aging* **1**, 769–782 (2021).
48. M. Legrand, S. Bell, L. Forni, M. Joannidis, J. L. Koyner, K. Liu, V. Cantaluppi, Pathophysiology of COVID-19-associated acute kidney injury. *Nat. Rev. Nephrol.* **17**, 751–764 (2021).
49. A. Subramanian, P. Tamayo, V. K. Mootha, S. Mukherjee, B. L. Ebert, M. A. Gillette, A. Paulovich, S. L. Pomeroy, T. R. Golub, E. S. Lander, J. P. Mesirov, Gene set enrichment analysis: A knowledge-based approach for interpreting genome-wide expression profiles. *Proc. Natl. Acad. Sci. U.S.A.* **102**, 15545–15550 (2005).
50. A. Liberzon, C. Birger, H. Thorvaldsdóttir, M. Ghandi, J. P. Mesirov, P. Tamayo, The Molecular Signatures Database (MSigDB) hallmark gene set collection. *Cell Syst.* **1**, 417–425 (2015).
51. E. Y. Chen, C. M. Tan, Y. Kou, Q. Duan, Z. Wang, G. V. Meirelles, N. R. Clark, A. Ma'ayan, Enrichr: Interactive and collaborative HTML5 gene list enrichment analysis tool. *BMC Bioinformatics* **14**, 128 (2013).
52. M. V. Kuleshov, M. R. Jones, A. D. Rouillard, N. F. Fernandez, Q. Duan, Z. Wang, S. Koplev, S. L. Jenkins, K. M. Jagodnik, A. Lachmann, M. G. McDermott, C. D. Monteiro, G. W. Gunderson, A. Ma'ayan, Enrichr: A comprehensive gene set enrichment analysis web server 2016 update. *Nucleic Acids Res.* **44**, W90–W97 (2016).
53. Z. Xie, A. Bailey, M. V. Kuleshov, D. J. B. Clarke, J. E. Evangelista, S. L. Jenkins, A. Lachmann, M. L. Wojciechowicz, E. Kropiwnicki, K. M. Jagodnik, M. Jeon, A. Ma'ayan, Gene set knowledge discovery with Enrichr. *Curr. Protoc.* **1**, e90 (2021).
54. B. Langmead, S. L. Salzberg, Fast gapped-read alignment with Bowtie 2. *Nat. Methods* **9**, 357–359 (2012).

**Acknowledgments:** We would like to thank the Haas and Zegar Family Foundations for enabling these studies. In addition, we would like to thank the genome technology center and pathology core of Mount Sinai and NYU Langone for services rendered. **Funding:** This work was funded entirely by the support of the Haas and Zegar Family Foundations. **Author contributions:** The study was designed by L.C., D.B.-M., and B.T. The experiments were performed by L.C., J.J.F., I.G., A.F., C.F.R., S.H., and T.R. Data analysis was performed by L.C., J.J.F., C.F.R., D.B.-M., and B.T. Preparation and writing of the manuscript was performed by L.C., J.J.F., J.M.M., and B.T. **Competing interests:** The authors declare that they have no competing interests. **Data and materials availability:** RNA-seq data collected here can be found on the NCBI Gene Expression Omnibus (GEO) under accession number GSE232204. All other data needed to evaluate the conclusions in the paper are present in the paper or the Supplementary Materials. None of the materials presented in this study require a material transfer agreement and can be provided upon direct request. This work is licensed under a Creative Commons Attribution 4.0 International (CC BY 4.0) license, which permits unrestricted use, distribution, and reproduction in any medium, provided the original work is properly cited. To view a copy of this license, visit <http://creativecommons.org/licenses/by/4.0/>. This license does not apply to figures/photos/artwork or other content included in the article that is credited to a third party; obtain authorization from the rights holder before using such material.

Submitted 4 January 2023

Accepted 26 May 2023

Published 13 June 2023

10.1126/scisignal.adg5470